ADVANCES IN MATERIALS SCIENCE, Vol. 23, No. 3 (77), September 2023

DOI: 10.2478/adms-2023-0017

Mariem Ben Hassen*, Seyyed Mojtaba Fakhari, Hatem Mrad

School of Engineering, University of Quebec in Abitibi-Témiscamingue (UQAT), Rouyn-Noranda, Canada

***** *mariem.benhassen@uqat.ca*

ASSESSMENT OF CRACK GROWTH AND FATIGUE LIFE OF AN AXIAL FAN BLADE BASED ON A CO-SIMULATION APPROACH

ABSTRACT

This paper presents static and dynamic stress analyses of an axial fan blade, which were carried out under real-life centrifugal and aerodynamic loading conditions using the Abaqus software. The location of the crack was identified on the pressure side of the blade at the conjunction between the blade and the blade root. It reveals a high agreement between the predicted location of stress distribution and the real origin of the crack location. Furthermore, a fracture mechanics criterion was adopted to simulate fatigue crack growth. This was performed using a fracture analysis FRANC3D code for three-dimensional problems. As a result, the calculated stress intensity factors (SIFs) were presented for the first steps, and the fatigue life of the fan blade was evaluated using the Forman de Koning model at different stress ratios.

Keywords: *Axial-fan-blade; Fatigue crack growth; Fatigue life; Stress ratios*

INTRODUCTION

The mining industry has notably played an essential role in the development of many countries. An estimation of 1.3% of the global workforce is involved in large and small-scale mining [1]. Thus, the mining industry must adapt and innovate exponentially to meet the multiple demands of this sector. In addition to adhering to the regulations imposed by the certification authorities regarding safety and toxic air emissions, the mining industry requires more efficient machines to improve reliability and minimize maintenance costs. In this context, ventilation system control plays a vital role in the safety of the mine production process. Ventilation in underground mines is a critical and widely regulated operation. As an example, controlling the airflow rate is required in a confined environment when the ambient air is contaminated by toxic gases (methane, dust, ammonia, etc.) from the mining process.

Ventilation not only involves significant energy costs but also has an impact on the respiratory and auditory health of miners. As one of the key mechanical components of rotating machinery, fan blades are often exposed to high mechanical stresses due to centrifugal forces and aerodynamic loads. During continuous operation in a hostile, high-stress environment, the first component that can potentially be damaged is the blade [2]. Under such severe operating conditions, the blades experience fatigue loads that lead to stress concentration at critical

Received 10 July 2023; Received in revised form 22 August 2023; Accepted 23 August 2023

locations where cracks can firstly initiate, grow under service loads, and finally result in the fracture of the blade. In engineering, fatigue fracture is among the most common forms of structural failure [3]. In the mining world, even a failure rate of one blade out of 1000 is unacceptable. It is necessary to prevent such premature fractures that might lead to huge economic losses and catastrophic accidents. Therefore, to guarantee the structure's safety, it is essential to accurately study the behavior of cracks in fan blades and predict their remaining operating life.

Despite the wide improvement in rotating machinery analysis, the difficulty of measuring deformation and vibration, and monitoring crack growth is not negligible. Thus, compared to time-consuming and high-cost experimental methods [4], numerical simulation methods, in particular the finite element method (FEM), are economical and powerful tools that have been proven to provide information about deformation, blade vibrations, and investigating fatigue crack growth. Several studies have been conducted on the numerical analysis of rotating machinery blades. Yu et al. [5] presented a fracture analysis of the impeller blade of a locomotive draught-fan using FEM. The results showed that under static loads the failure did not occur at the stress concentration area, and the mechanical resonance of the blades did not contribute to blade failure. In contrast, the analysis of Zhao et al. [6] and Poursaeidi et al. [7], showed that the crack occurred at the same location as the maximum stress area, and that resonance was the primary reason for the fatigue fracture in both a motor cooling fan blade and an R1 compressor blade.

The conventional finite element technique requires a very fine mesh at the crack tip to simulate crack growth, while it is also important to constantly update the structural configuration and re-mesh. However, this is challenging due to the complexities of crack surface morphology [4]. In recent years, with the progress in finite element analysis and modeling, fatigue crack growth (FCG) prediction based on analytical models and the employment of computational software has become important. Remadi et al. [8] used ABAQUS for predicting the fatigue crack growth of 2024-T3 aluminum alloys under variable-amplitude loading. When the direction of the crack growth path is known beforehand, the virtual crack closure technology (VCCT) [9] and the cohesive zone model(CZM) techniques [10] are appropriate. In addition, common fracture analysis codes for three-dimensional problems, such as the extended finite element modeling (XFEM) module in ABAQUS [4,11], MSc Fatigue, and FRANC3D, are now at hand to study the behavior of FCGs in rotating structures without requiring meshing refinement at the crack tip, neither remeshing while the crack is propagating.

FRANC3D has been adopted due to its strengths in crack growth simulations. Riddell et al. [12] revealed that FRANC3D provides a higher correlation for fatigue crack growth. Poursaeidi et al. [13] investigated two semi-elliptical cracks on the fracture surface. They simulated FCG using FRANC3D for both one-crack and two-crack cases. Blade life in that study was calculated with the Paris model equation [14] and the NASGRO equation according to Forman-Newman-De Koning (FNK) [15]. Mangardich et al. [16] used the same NASGRO equation to model crack growth and predict the crack propagation life of an aircraft engine in a high-pressure compressor blade under combined high cycle fatigue (HCF) and low cycle fatigue (LCF) loading. Malipatil et al. [17,18] studied the fatigue crack growth behavior of a nickel base superalloy of GTM720 and GTM718, respectively. In their first work, the fatigue crack growth behavior was predicted with a cycle-by-cycle approach under spectrum load cycles approaches using Paris and Walker [19] equations. A comparison between numerical and experimental results showed a fairly good correlation. In their second study, the FCG behavior was established using two stress ratio effect laws: Paris-Walker(P-W) and Bi-linear-Walker(B-W) in FRANC3D in conjunction with MSC NASTRAN.

The rest of this article is structured as follows. In the first part, a static structural analysis was conducted to evaluate the stress distribution on the blade with a focus on the maximum stress area. Then, a modal analysis was carried out to determine the dynamic mode shapes and to verify if there was any risk of resonance. In the second part, the stress analysis was imported into the FRANC3D code for crack growth modeling purposes, where an initial crack was inserted and grown based on the maximum tensile stress theory. The stress intensity factors (SIFs) of first mode cracks were calculated and the fatigue life under analyzed stress was predicted using the NASGRO equation with different stress ratios.

The axial fan studied in this work was a 42-inch axial fan model, as shown in Fig. 1, where the blade/hub bounding was constructed using a U-bolt. During operation, a problem occurred, and an emergency led to stop the axial-fan. After investigation it was determined that, one by one, the axial fan blades were pulled out of their roots.

Fig. 1. Axial fan model

MATERIALS AND METHODS

Fractography and visual observation

An investigation of the fractured fan blades showed that the cracks initiated at the same place for all the blades. Fractography and visual observations were conducted for the fractured fan blades, as received. Fig. 2 shows a top view of the cracked blade that provoked this study, which shows the final step of the crack propagation area on the conjunction region between blade and the blade root. Once the crack reached a critical depth, its growth became unstable, resulting in the collision between the blade and the root due to overload failure and the domination of the shear stress in a plane of 45 degrees at the final fracture area.

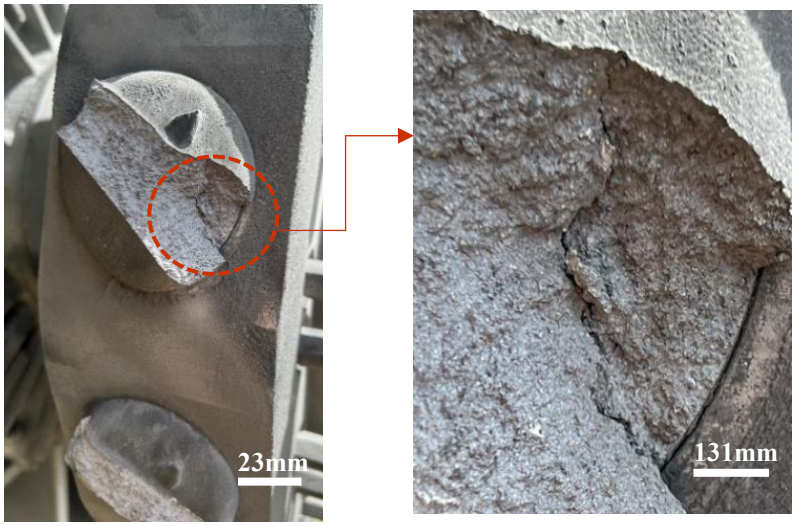

Fig. 2. Final fracture crack surface of the blade

Finite element modeling

The finite element bladed fan was a cyclic-symmetric structure consisting of 15 blades. However, to minimize the required resources and analysis time consuming, an assembly with a single blade was imported to the ABAQUS finite element code. The mesh type and mesh size were adapted to ensure convergence based on numerical stability and consistence criterion of running model [20]. An optimum mesh of 45,033 elements and 69,404 nodes was selected. The 10-node quadratic tetrahedron element (C3D10) was used in this study. As the blades were subjected to static and dynamic loads, static stress and modal analysis of the blade was performed in this study.

A static structural analysis was performed to determine the static stress distribution. The mechanical property material of the blade is an aluminium alloy AL 2024-T86, with the following mechanical properties: an elasticity modulus of 717×10^2 MPa, a density of 2,768 kg/m^3, a Poisson's ratio of 0.33, an ultimate tensile strength of 399.91 MPa, and a yield strength of 386.12 MPa.

The blade root translation and rotation were constrained in all directions. Two main sources of stress exist for rotating blades: centrifugal forces and aerodynamic forces. In this analysis, centrifugal forces were simulated by applying a rotating condition with an operational impeller speed of 1,800 rpm. To investigate the aerodynamic forces, three approaches can be considered: experimental models, turbo-machine theory, and computational fluid dynamics (CFD) [7]. According to CFD analysis, distributed aerodynamic equilibrium pressure was computed and applied gradually from the root to the tip of the blade using values from 83.2 kPa to 110 kPa. Once the numerical model has been created, and the boundary conditions and loads were set, the stress analysis was then established; the von Mises stress was chosen to evaluate the stress state of the axial-flow mining fan, which is defined as follows [6]:

$$\sigma_{von-Mises} = \sqrt{\frac{(\sigma_1-\sigma_2)^2+(\sigma_2-\sigma_3)^2+(\sigma_3-\sigma_1)^2}{2}} \quad (1)$$

where σ_1 is the maximum principal stress, σ_2 is the middle principal stress, and σ_3 is the minimum principal stress.

Fig. 3. The maximum stress was located at the root area of the blade, which was due to the non-uniform stress distribution in that location. As illustrated in in Fig. 3 the maximum static stress at the blade reached a value of 182.1 MPa. The von Mises stress distribution on the pressure side of the blade is presented; the local stress concentration area at the intersection of blade/roots reveals a high agreement between the predicted stress distribution and the real origin of the crack location shown in Fig. 2.

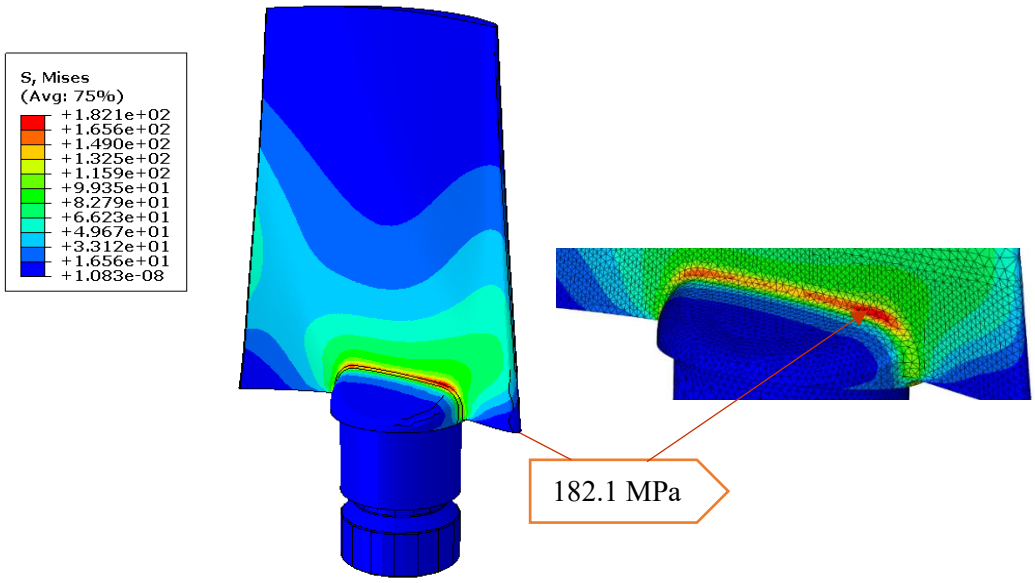

Fig. 3. Von Misses stress distribution under static loads at the pressure side of the blade

Modal analysis provides the vibrational characteristics (natural frequencies, damping properties and mode shapes) of the blade structure. The general form of governing equations for the entire blade can be written as:

$$M\ddot{x} + C\dot{x} + Kx = F(t) \tag{2}$$

where M, C, and K are the total mass matrix, the total damping matrix, and the total stiffness matrix, respectively; x is the displacement vector; $\dot{x}$ is the velocity vector; $\ddot{x}$ is the acceleration vector; and F(t) is the dynamic load vector. To determine the dynamic characteristic, a modal analysis was performed on the structure.

The damping matrix is generally neglected in the numerical modal analysis [21]. The undamped free vibration equation derived from Eq. (2) can be expressed as:

$$M\ddot{x} + Kx = 0 \tag{3}$$

By substituting the particular solution of $x = \varphi e^{jwt}$ into Eq. (3), we obtain:

$$(K - w^2 M)\varphi = 0 \tag{4}$$

This is a generalized eigenvalue problem; the eigenvalues $w_i{}^2$ ($1 \leq i \leq n$) and model shape can be obtained by solving:

$$det(K - w^2 M) = 0 \tag{5}$$

Thus, the relationship between natural frequency, structure stiffness and mass can be expressed as follows:

$$f_i = \frac{1}{2\pi}\sqrt{\frac{K_i}{M_i}}, \qquad i = 1,2,3 \ldots., n \tag{6}$$

where f_i is the natural frequency of the structure, K_i is the stiffness of the structure and M_i is the structure mass.

A modal analysis was carried out to study the dynamic behavior of the blade and to check if the mechanical resonance of the blades contributed to blade failure. Damping was not considered. The first six mechanical natural frequencies and mode shapes calculated using numerical modal analysis are shown in

Table 1.

Table 1. *First five blade natural frequencies at different rotation speeds (Hz)*

Mode number	Natural frequency (rad/s)					
	0	50	100	150	200	250
Mode 1	313.85	313.73	313.36	312.76	311.91	310.84
Mode 2	850.71	850.74	850.81	850.94	851.11	851.32
Mode 3	1,284.3	1,284.7	1,285.8	1,287.7	1,290.3	1,293.7
Mode 4	1,708.9	1,708.9	1,709.1	1,709.2	1,709.5	1,709.8
Mode 5	2,248.8	2,248.9	2,249.2	2,249.7	2,250.4	2,251.4

The magnitude distributions for the first three modes are shown in Fig. 4. The first three natural frequencies of the blade were 313.68 Hz, 851.02 Hz, and 1,289.4 Hz. There was a stress concentration field at the root/blade intersection, as shown in Fig. 5, which shows a good agreement with the fractography observations of the fractured blade.

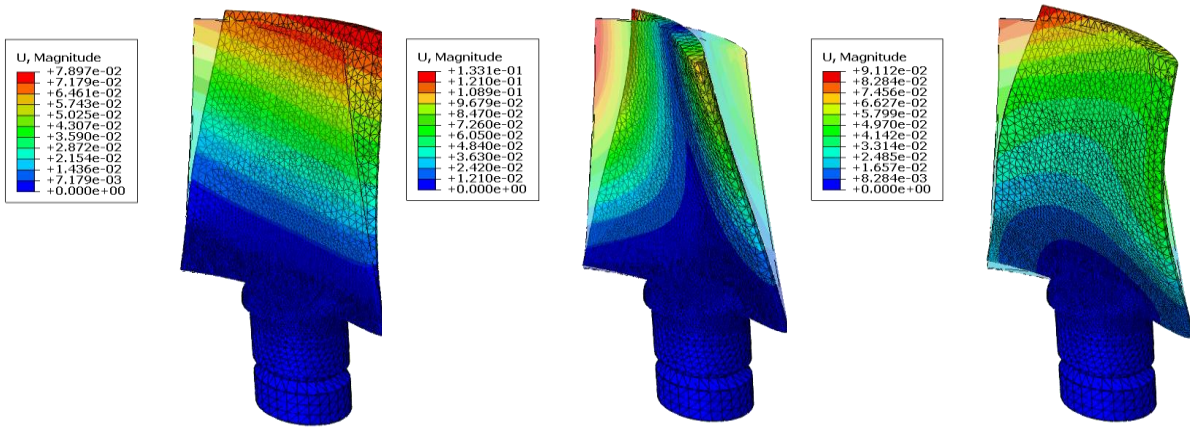

(a) **(b)** **(c)**

$f_I = 313.68$ Hz $f_{II} = 851.02$ Hz $f_{III} = 1{,}289.4$ Hz

Fig. 4. Magnitude distribution under the three first natural mode shapes of the blade: (a) first mode, (b) second mode and (c) third mode

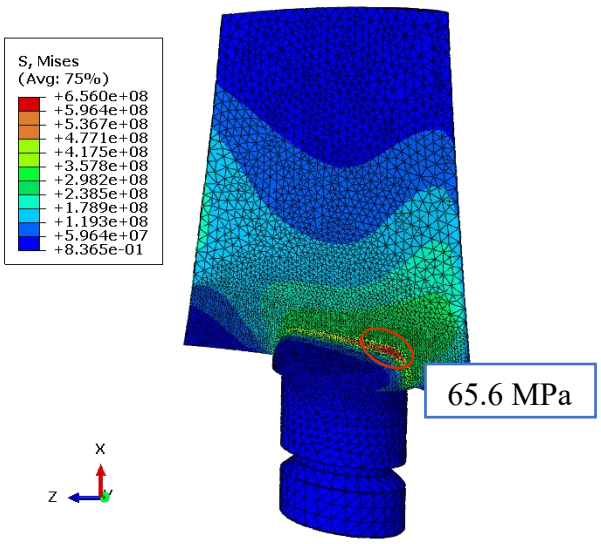

Fig. 5. Stress concentration area of the blade under the first natural mode shape

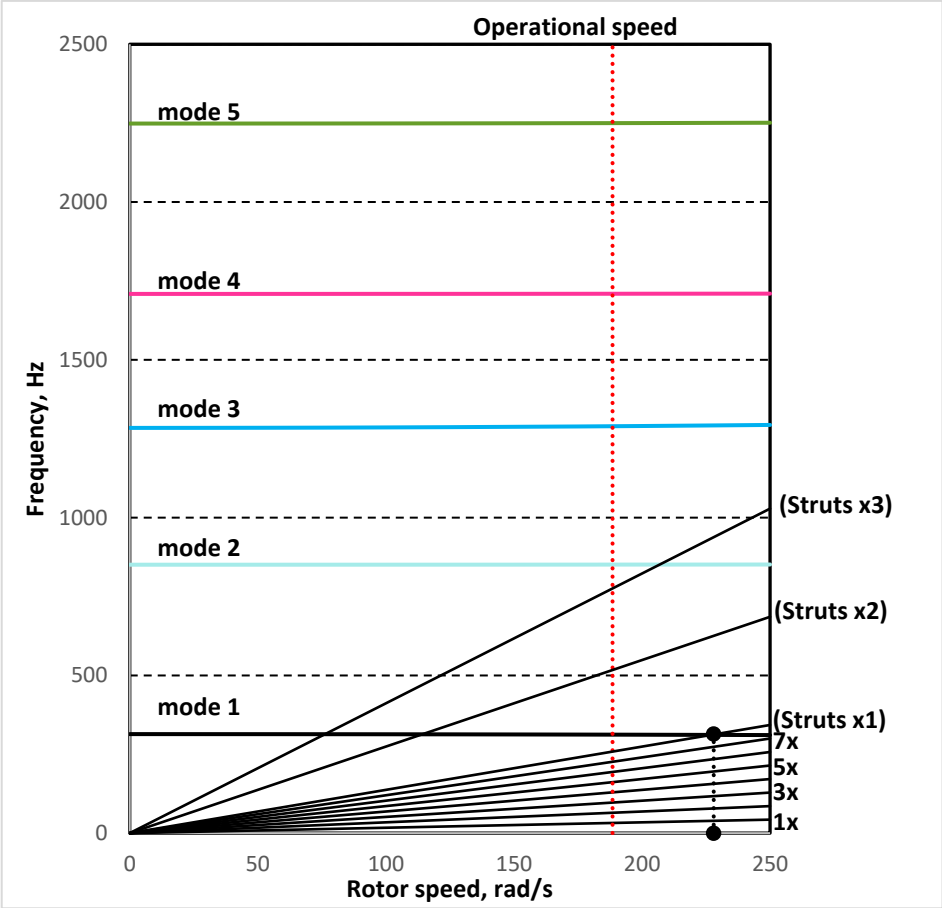

Fig. 6. Campbell diagram

The Campbell diagram shown in Fig. 6 constructed using the first five natural frequency magnitudes through various rotor speeds (0-250 rad/s). However, Fig. 6 shows that there was a coincidence between the first 8th harmonic order and the first natural frequency of the blade at a rotor speed equal to 228 rad/s. So, this speed was considered as a critical rotor speed at which there was a high probability of fracture due to resonance.

None of the first five mechanical natural frequencies coincided with any harmonic orders at the operational speed of 188.5 rad/s (1800 rpm). It was concluded at that rated rotor speed, the probability of fracture due to resonance was low.

Numerical fracture analysis

In general, in the fracture mechanics domain, crack growth models can be divided into global and cycle-by-cycle analysis. The difference between the models is that global analysis predicts fatigue crack growth using the average of all applied loading cycles [21,22], whereas cycle-by-cycle analysis considers the crack growth of each cycle separately, then, by accumulation, determines the crack growth life. Cycle-by-cycle analysis was carried out in this study. Many laws have been established to describe the evolution of fatigue crack propagation. The simplest expression used by engineers in the last fifty years, which is well-known to predict fatigue crack propagation, is a power law described by Paris and Erdogan [23], known as the Paris law:

$$\frac{da}{dN} = C\Delta K^m \tag{7}$$

where a is the length of the crack, da/dN is the crack propagation rate, ΔK is the range of applied stress intensity factors (SIF) defined as $K_{max} - K_{min}$, and C and m are two material parameters defining, respectively, the position and the slope of the line on the log-log plot of da/dN versus ΔK. As mentioned below, the Paris law is the classical formula for fatigue life prediction as it does not consider overload retardation, the effect of stress ratio [24], and interaction effects.

The Forman de Koning (FNK) (NASGRO) model was used in this study, as it has many advantages compared to other existing models. The FNK equation considers the fatigue threshold value, the fatigue fracture toughness effects, and the crack closure effects with a better match for various load ratios [25]. It is expressed as follows:

$$\frac{da}{dN} = C\left(\frac{(1-f)}{(1-R)}\,\Delta K\right)^n \frac{\left(1-\frac{\Delta K_{th}}{\Delta K}\right)^p}{\left(1-\frac{K_{max}}{K_C}\right)^q} \tag{8}$$

where N is the number of applied load cycles, ΔK is the SIF range, K_{max} is the stress intensity factor corresponding to the maximum applied load, R is the stress ratio, and p, q, C, and n are empirical coefficients.

The variable f represents the crack closure function that takes the stress ratio's impact into account, defined according to Newman's crack closure phenomenon as [26]:

$$f = \begin{cases} max(R, A_0 + A_1R + A_2R^2 + A_3R^3) & R \geq 0 \\ A_0 + A_1R & -2 \leq R < 0 \end{cases} \tag{9}$$

where:

$$A_0 = (0.825 - 0.34\alpha + 0.05\alpha^2)\left[cos\left(\frac{\pi}{2}\frac{S_{max}}{\sigma_0}\right)\right]^{\frac{1}{\alpha}}$$

$$A_1 = (0.415 - 0.071\alpha)\frac{S_{max}}{\sigma_0}$$

$$A_2 = 1 - A_0 - A_1 - A_3$$

$$A_3 = 2A_0 + A_1 - 1$$

where α is the plane stress/strain constraint factor; and s_{max}/σ_0 is the ratio of the maximum applied stress to the flow stress. The fatigue threshold ΔK_{th} in Eq. (8) (the threshold SIF range) for varying R-ratios is expressed as [26]:

$$\Delta K_{th} = \begin{cases} \dfrac{\Delta K_0 \sqrt{\dfrac{a}{a+a_0}} \left[\dfrac{1-R}{1-f}\right]^{(1+RC_{th}^P)}}{(1-A_0)^{(1-RC_{th}^P)}} & R \geq 0 \\ \dfrac{\Delta K_0 \sqrt{\dfrac{a}{a+a_0}} \left[\dfrac{1-R}{1-f}\right]^{(1+RC_{th}^m)}}{(1-A_0)^{(C_{th}^P-RC_{th}^m)}} & R < 0 \end{cases} \tag{10}$$

where ΔK_0 is the threshold SIF range, a is the crack length, a_0 is a fixed small crack parameter, C_{th} is an empirical constant that has different values and K_C, in Eq.(8), is the critical stress intensity factor, also named as, the fracture toughness of the material, the expression for this is [26]:

$$K_c = K_{Ic}(1 + B_k e^{-\left(A_k \frac{t}{t_0}\right)^2}) \tag{11}$$

$$t_0 = 2.5 \left(\frac{K_{Ic}}{\sigma_{ys}}\right)^2 \tag{12}$$

where K_{Ic}, t_0, t, σ_{ys}, A_k, and B_k, are, respectively, fracture toughness, reference thickness (plain strain condition), thickness, tensile strength yield, and fit parameters.

Algorithm flowchart of crack growth simulation and fatigue life prediction

Fig. 7 shows the fatigue crack growth flowchart of the numerical approach used in this step. It can be described as follows: first, based on FEM analysis for the target structure using ABAQUS, the input file was imported into FRANC3D with input data of the material and boundary conditions with or without retaining the mesh sets/surfaces.

Next, a New Flaw Wizard semi-elliptical surface crack with an advanced angle threshold of 168, an aspect ratio (a/c) of 1, and an initial crack length (a_0) was inserted. The initial crack shape and size were assumed to be a semi-elliptical surface crack with a = c = 2.5 mm, as shown in Fig. 8, where a and c are the semi-axes of the ellipse whose centre is at the origin of the coordinate system [27]. This assumption was based on several investigations of failure analysis of blades, such as in the work of Lieu et al. [28], Branco et al. [27] and Witek [29].

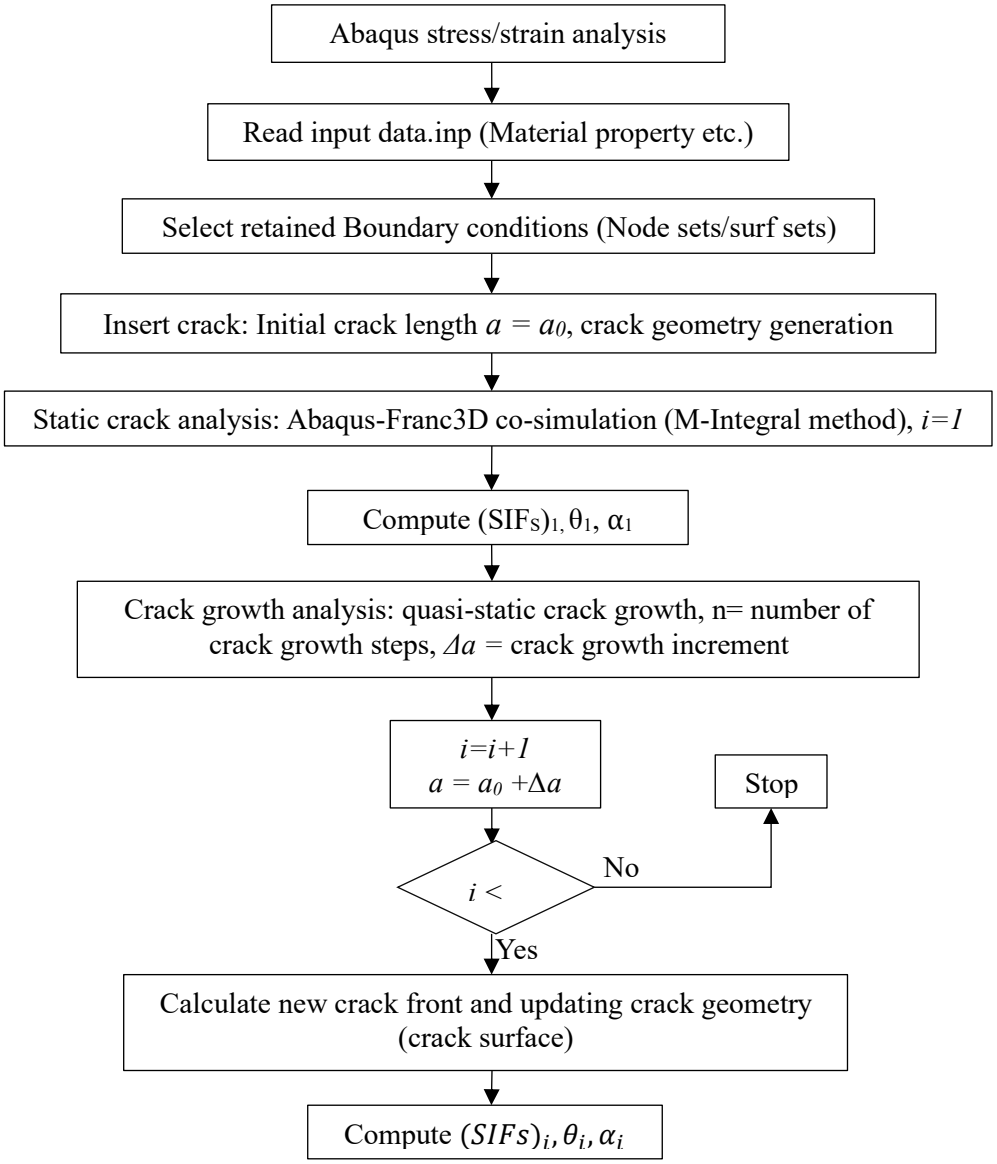

Fig. 7. Schematic flowchart part I: crack growth simulation

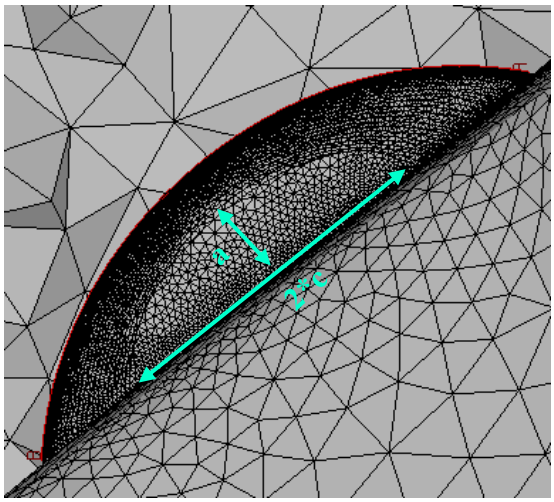

Fig. 8. Initial crack shape and the crack paths

$$
\begin{aligned}
J^{(1+2)} &= J^{(1)} + J^{(2)} + M^{(1,2)} \\
&= \left[\frac{1-\vartheta^2}{E}(K_I^{(1)})^2 + \frac{1-\vartheta^2}{E}(K_{II}^{(1)})^2 + \frac{1+\vartheta}{E}(K_{III}^{(1)})^2\right] \\
&+ \left[\frac{1-\vartheta^2}{E}(K_I^{(2)})^2 + \frac{1-\vartheta^2}{E}(K_{II}^{(2)})^2 + \frac{1+\vartheta}{E}(K_{III}^{(2)})^2\right] \\
&+ \left[\frac{1-\vartheta^2}{E}K_I^{(1)}K_I^{(2)} + \frac{1-\vartheta^2}{E}K_{II}^{(1)}K_{II}^{(2)} + \frac{1+\vartheta}{E}K_{III}^{(1)}K_{III}^{(2)}\right]
\end{aligned} \tag{13}
$$

$$
M^{(1,2)} = \frac{1-\vartheta^2}{E}K_I^{(1)}K_I^{(2)} + \frac{1-\vartheta^2}{E}K_{II}^{(1)}K_{II}^{(2)} + \frac{1+\vartheta}{E}K_{III}^{(1)}K_{III}^{(2)} \tag{14}
$$

Later, according to the given crack growth step size (crack growth increment), the crack growth analysis was conducted.

The new geometry and new crack surface were updated (update of the initial crack length, a, and the initial crack slant angle, θ). The FRANC3D code was used for SIF calculations and ABAQUS software was used for updating the stress after each crack growth. Generally, the majority of cracks occurring in complex engineering structures are mixed mode. Numerous criteria have been developed to govern the crack propagation direction and growth rates in mixed mode situations [30], such as the maximum energy release rate (MERR) [31], the minimum strain energy density criterion [32], and the circumferential tensile stress/hoop criterion (MTS) [33]. In this study, the MTS criterion was adopted. Using the generated stress intensities, as reported by the linear finite element method (LFEM) [34], the kink angle and the local extension for each node along the crack front were predicted as follows [4]:

$$
\theta = \frac{1}{\sqrt{2\pi r}}\ cos\frac{\theta}{2}\left(K_I cos^2\frac{\theta}{2} - \frac{3}{2}\ K_{II} sin\theta\right) \tag{15}
$$

To realize the crack propagation, the process was automatically repeated until reaching the predefined number of crack growth steps.

The second part of the flowchart describes the relationship between the crack growth length and the number of load cycles under a cyclic-constant magnitude loading. Based on the appropriate growth rate model, the crack growth length under each load cycle was evaluated. For the fatigue life calculation module, the fatigue life statistics ends when either the maximum SIF cross the critical SIF value, or the predefined number of cycles (N) is reached. Based on the cycle-by-cycle SIFs algorithm, the crack growth simulation module and the fatigue life prediction module were deftly coupled.

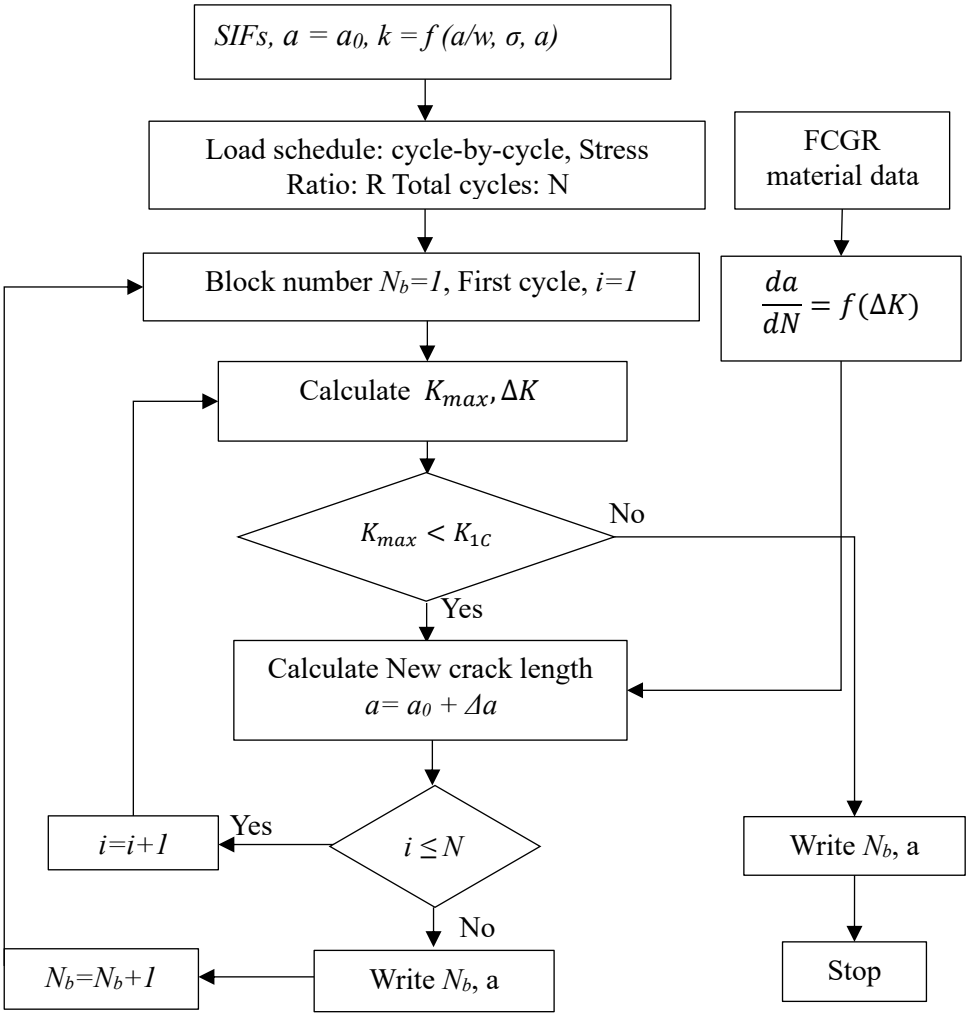

Fig. 9. Schematic flowchart part II: fatigue life prediction

RESULTS AND DISCUSSION

Case study

From the original finite element model, a smaller defined volume of parts was extracted to create a sub-model for crack growth analysis. The crack front's initial shape was assumed to be semi-elliptical.

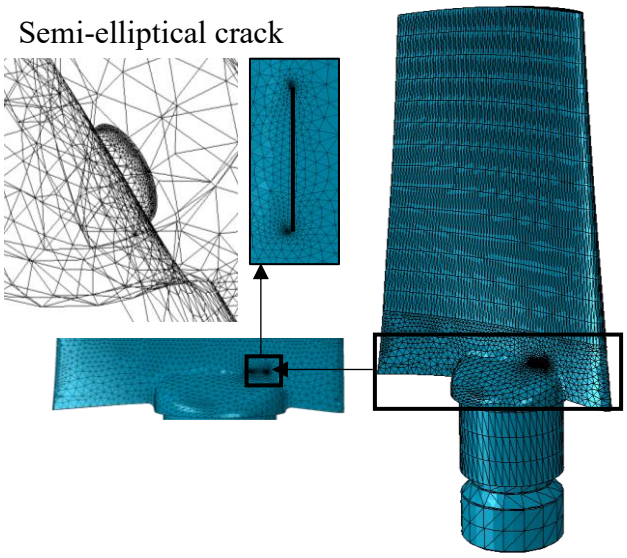

Fig. 10. The original model, sub-model, and crack insertion area

An initial semi-elliptical crack with a surface length c = 2.5 mm and an aspect ratio a/c=1 was inserted into the sub-model, parallel to the blade axis at the peak stress location. After that, the sub-model was meshed and reinserted into the complete FEA model with the original FEA mesh and boundary nodes. The fracture mechanics model created based on the finite element mesh is shown in Fig. 10.

Fatigue crack growth analysis

According to part I of the flowchart for crack growth simulation in Fig. 7, before starting the simulation, a fixed crack growth increment must be defined. Theoretically, the use of a small crack growth increment provides greater accuracy for the crack growth path, but it is more computationally expensive compared to a large crack growth increment [4]. The crack growth increment was chosen to be $\Delta a = 0.1mm$ based on trial tests considering the calculation efficiency (time- precision ratio) [35]. In this study, 183 points were used to generate the initial crack front, and after each growth step the number of points increased.

After inserting the crack and defining the crack growth increment, SIFs along various crack fronts were calculated at each discrete point using the M-integral method [36]. The calculation results are shown in Fig. 11. This figure illustrates, the Mode I, Mode II, and Mode III SIFs along the fracture front for the first 40 crack iterations, computed using FRANC3D code.

The magnitude of the Mode I SIFs along the fracture front increased as the crack extended maintaining the same shape. The complex crack growth was reflected by the variation in Mode I, where the lowest K_I values were located at the middle of the crack and increased on both sides. For Mode I, maximum SIFs were located near the crack endpoints and minimum SIFs were located at maximum crack depth. In Mode II, there was a kink in the first step, so the SIF along the crack front for the initial crack was non-zero, whereas the rest of the crack iterations expanded to fulfill the MTS theory.

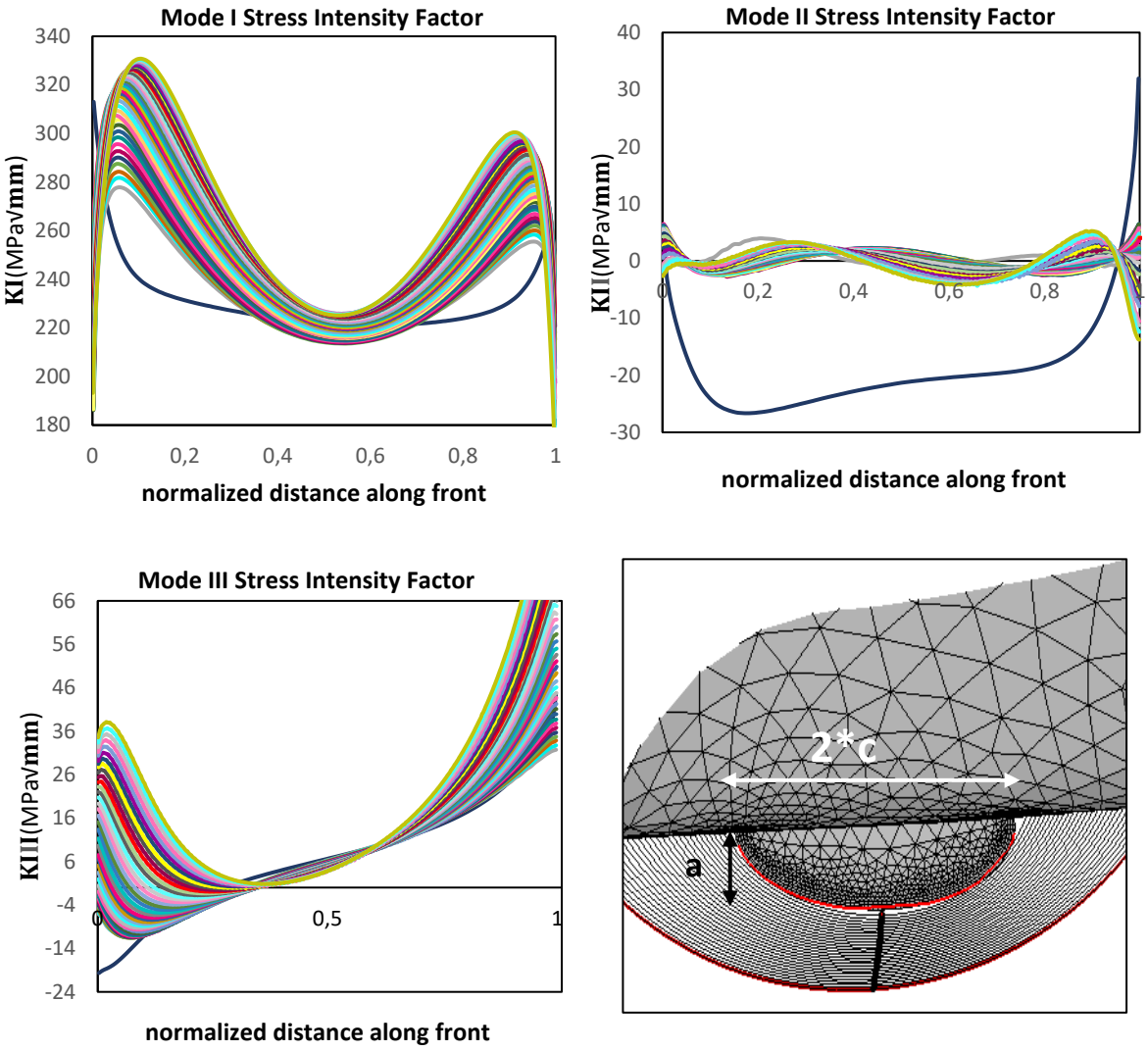

Fig. 11. Mode I, Mode II, and Mode III stress intensities along the first 40 crack fronts and the simulated crack propagation path by FRANC3D code

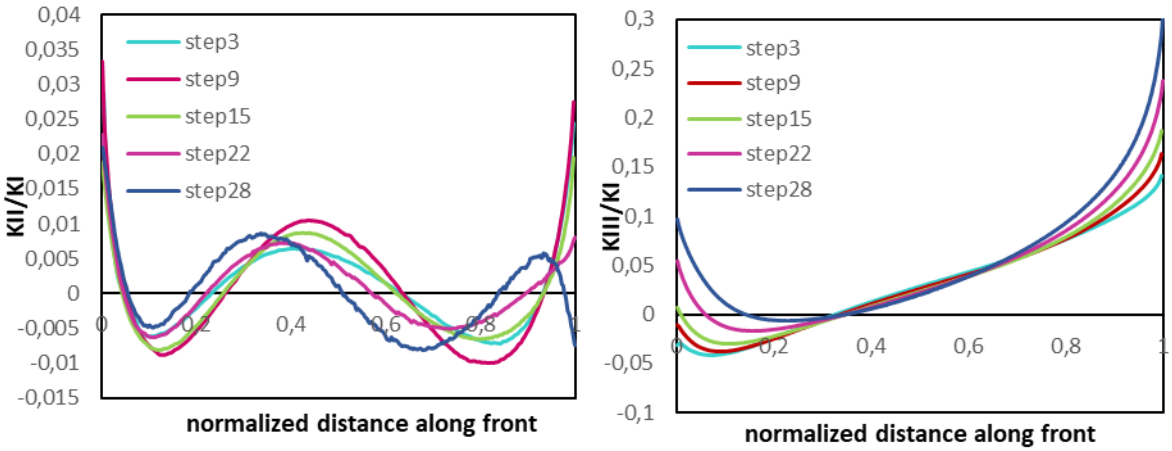

Fig. 12. Comparison between K_I and: K_{II} on the left and K_{III} on the right

Fig. 12 illustrates the SIF ratios for various crack front steps for K_{II}/K_I and K_{III}/K_I. Even though the value of Mode I SIF was dominant, the Mode II and Mode III SIF's were not negligible. As the magnitude of the interference increased, the SIF values of Mode II and Mode III had a greater extent, and the crack front became more multiaxial. The negative SIF values demonstrated the evolution of crack fronts in the compressive state [37].

Fatigue life prediction

The NASGRO fatigue crack growth model shown in Eq. (8) was adopted for crack life prediction. The crack growth parameters for the 2024-T861 aluminum alloy from the FRANC3D material database are illustrated in Table 2.

The fatigue crack growth life was calculated for four different stress ratios R = 0.1, 0.2, 0.3, and 0.4. As can be seen from the results shown in Fig. 13, the life cycle was significantly dependent on the stress ratio. When the stress ratio R = 0.1, the initial crack of 0.1mm-long crack extended to 3.165 mm with a predicted life cycle of 248880 cycles from initiation; when the stress ratio R = 0.4, the initial 0.1mm crack extended to the same length of 3.165 mm with a predicted life cycle of 1.57E+06 cycles.

Table 2*.Mechanical properties and fatigue crack growth parameters used to predict fatigue crack growth behavior of 2024-T861 Al used in axial fan blades*

Mechanical properties of 2024-T861 Al	
Elasticity modulus, E [MPa]	71,700
Density, ρ [Kg/mm^3]	$2.768 * 10^{-6}$
Poisson's ratio, ν	0.336
Fatigue crack growth parameters	FNK Model
Crack growth coefficient, C [mm/ (cycle$*$ (MPa $\sqrt{m})^{3.81}$)]	$7.58 * 10^{-12}$
Crack growth exponent, n [-]	3.181
Threshold SIF range, ΔK_0 [MPa $\sqrt{mm}$]	97.3
Fracture toughness, K_{Ic} [MPa $\sqrt{mm}$]	1,251
Tensile strength, UTS [MPa]	399.91
Yield strength, Yield [MPa]	386.12
Fixed small crack parameter, a_0 [mm]	0.0381
Plain stress/strain constraint factor, α	1.5
Ratio of the maximum applied stress to the flow stress, $\frac{S_{max}}{\sigma_0}$	0.3
Fit parameter, A_k	1
Fit parameter, B_k	1
Empirical constant, C_{th}	1.5

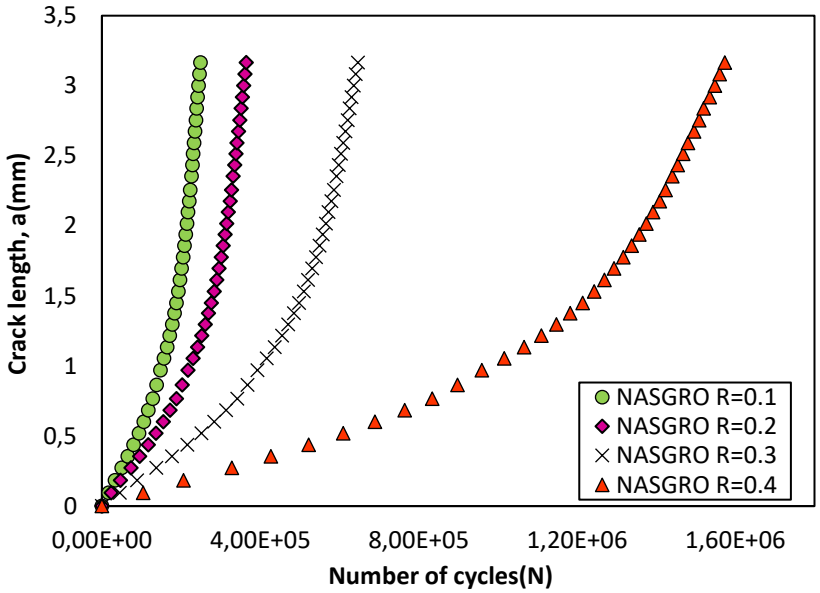

Fig. 13. Fatigue crack growth life curves under different stress ratios

CONCLUSIONS

Based on the finite element analysis, and the study carried out using numerical fracture software, the conclusions were as follows:

- Static stress and modal analysis were performed under real life centrifugal and aerodynamic loading conditions. The location of the crack in the axial fan blade was identified on the pressure side of the blade at the conjunction between the blade and the blade root with a maximum of 182.1 MPa von Mises stress. The results of the finite element analysis were used as input for the FRANC3D code.
- The displacement approach was applied to calculate the stress intensity factors for three fracture modes. The Forman-Newman-de Koning crack growth model was used for predicting axial-fan-blade fatigue crack life under different stress ratios. The results have shown that the life cycle significantly depended on the stress ratio.

As future work, the fatigue crack growth model used in this study can be-compared with specials models such as, the load interaction models, as they consider the variable amplitude loading and the overload applied on structural components in rotating machines. In addition, as an extension of this study, an experimental data collection system using online sensors will be installed on an axial fan in service to collect real-world date which will be compared with this work for validation.

ACKNOWLEDGEMENT

We appreciate the Natural Sciences and Engineering Research Council of Canada's support (NSERC). This work is additionally supported by the industrial partner Hyperflo, 100 Jacques-bibeau, Rouyn-Noranda, QC, J9Y 0A3. The authors would like to thank Omar Ibrahim and Bruce J. Carter from Fracture Analysis Consultants (FAC) for their advice on crack growth simulations.

Conflicts of Interest

The authors declare that they have no competing financial interests or personal relationships that could have seem to influence the study reported in this paper.

REFERENCES

1. Azapagic A. Developing a framework for sustainable development indicators for the mining and minerals industry. J Clean Prod. 2004;12:639–62.
2. Witek L, Wierzbińska M, Poznańska A. Fracture analysis of compressor blade of a helicopter engine. Eng Fail Anal. 2009;5:1616–22.
3. Stephens RI, Fatemi A, Stephens RR, Fuchs HO. Metal Fatigue in Engineering. John Wiley & Sons; 2000.
4. Chen Z, Bao H, Dai Y, Liu Y. Numerical prediction based on XFEM for mixed-mode crack growth path and fatigue life under cyclic overload. Int J Fatigue. 2022;162:106943.
5. Yu Z, Xu X, Guo J, Cai T. Fracture analysis of impeller blade of a locomotive draught-fan. Eng Fail Anal. 2013;27:16–29.
6. Zhao Y, Feng J, Zhou Q, Peng X. Blade fracture analysis of a motor cooling fan in a high-speed reciprocating compressor package. Eng Fail Anal. 2018;89:88–99.
7. Poursaeidi E, Babaei A, Mohammadi Arhani MR, Arablu M. Effects of natural frequencies on the failure of R1 compressor blades. Eng Fail Anal. 2012;25:304–15.
8. Remadi A, Bahloul A, Bouraoui C. Prediction of fatigue crack growth life under variable-amplitude loading using finite element analysis. Comptes Rendus Mécanique. 2019;347:576–87.
9. Xie D, Biggers SB. Strain energy release rate calculation for a moving delamination front of arbitrary shape based on the virtual crack closure technique. Part I: Formulation and validation. Eng Fract Mech. 2006;73:771–85.
10. Russo R, Chen B. Overcoming the cohesive zone limit in composites delamination: modeling with slender structural elements and higher-order adaptive integration. Int J Numer Methods Eng. 2020;121:5511–45.
11. Gibert G, Prabel B, Gravouil A, Jacquemoud C. A 3D automatic mesh refinement X-FEM approach for fatigue crack propagation. Finite Elem Anal Des. 2019;157:21–37.
12. Riddell WT, Ingraffea AR, Wawrzynek PA. Experimental observations and numerical predictions of three-dimensional fatigue crack propagation. Eng Fract Mech. 1997;58:293–310.
13. Poursaeidi E, Bakhtiari H. Fatigue crack growth simulation in a first stage of compressor blade. Eng Fail Anal. 2014;45:314–25.
14. Paris P. C; ERDOGAN, F: A critical analysis of crack propagation laws. J Basic Eng. 1963;85:528–34.
15. Forman RG. Study of fatigue crack initiation from flaws using fracture mechanics theory. Eng Fract Mech. 1972;4:333–45.
16. Mangardich D, Abrari F, Fawaz Z. Modeling crack growth of an aircraft engine high pressure compressor blade under combined HCF and LCF loading. Eng Fract Mech. 2019;214:474–86.
17. Malipatil SG, Nagarajappa N, Majila AN, Chandru Fernando D, Bojja R, Jagannathan N, et al. A study on the fatigue crack growth behaviour of GTM718 nickel based super alloy under cold-TURBISTAN spectrum loads. Theor Appl Fract Mech. 2022;120:103386.

18. Malipatil SG, Majila AN, Chandru Fernando D, Manjuprasad M, Manjunatha CM. Fatigue crack growth behaviour of a nickel base super alloy GTM720 under cold-TURBISTAN spectrum load sequence. Theor Appl Fract Mech. 2021;112:102913.

19. Ahmad A. Mechanical Vibrations Fifth Edition. [cited 2023 Jan 4]; Available from: https://www.academia.edu/44772271/Mechanical_Vibrations_Fifth_Edition

20. Layachi M, Khechai A, Ghrieb A, Layachi S. Numerical Failure Analysis of Laminated Beams Using a Refined Finite Element Model. Adv Mater Sci. 2023;23:32–57.

21. Rao: Mechanical vibrations laboratory manual - Google Scholar [Internet]. [cited 2022 Sep 6]. Available from: https://scholar.google.com/scholar_lookup?title =Mechanical%20Vibrations&publication_year=2010&author=S.S.%20Rao

22. Khan S, Alderliesten R, Schijve J, Benedictus R. On the fatigue crack growth prediction under variable amplitude loading. 2007;

23. Paris P, Erdogan F. A Critical Analysis of Crack Propagation Laws. J Basic Eng. 1963;85:528–33.

24. Beden S, Abdullah S, Ariffin AK. Review of Fatigue Crack Propagation Models for Metallic Components. Eur J Sci Res. 2009;28.

25. NASGRO® Software Overview [Internet]. Southwest Res. Inst. 2017 [cited 2023 Jan 4]. Available from: https://www.swri.org/nasgro-software-overview

26. Mettu SR, Shivakumar V, Forman RG, McMahon JJ, Johnson N, Newman JC, et al. NASGRO 3.0 - A software for analyzing aging aircraft.

27. Branco R, Antunes FV, Costa JD, Yang FP, Kuang ZB. Determination of the Paris law constants in round bars from beach marks on fracture surfaces. Eng Fract Mech. 2012;96:96–106.

28. Liu H, Yang X, Li S, Shi D. A numerical approach to simulate 3D crack propagation in turbine blades. Int J Mech Sci. 2020;171:105408.

29. Witek L. Experimental Crack Propagation Analysis of the Compressor Blades Working in High Cycle Fatigue Condition. Fatigue Aircr Struct. 2009;2009:195–204.

30. Kim J-H, Paulino GH. On Fracture Criteria for Mixed-Mode Crack Propagation in Functionally Graded Materials. Mech Adv Mater Struct. 2007;14:227–44.

31. Palaniswamy K, Knauss WG. Propagation of a crack under general, in-plane tension. Int J Fract Mech. 1972;8:114–7.

32. Sih GC. Strain-energy-density factor applied to mixed mode crack problems. Int J Fract. 1974;10:305–21.

33. Erdogan F, Sih GC. On the Crack Extension in Plates Under Plane Loading and Transverse Shear. J Basic Eng. 1963;85:519–25.

34. Anderson TL. Fracture Mechanics: Fundamentals and Applications, Fourth Edition. 4th ed. Boca Raton: CRC Press; 2017.

35. Xiaotong Y, Robuschi S, Fernandez I, Lundgren K. Numerical assessment of bond-slip relationships for naturally corroded plain reinforcement bars in concrete beams. Eng Struct. 2021;239:112309.

36. Hou J, Lv J, Ricoeur A, Hu Y, Zuo H, Chen Y, et al. The M-integral in fracture and damage mechanics: A review of developments and applications. Eng Fract Mech. 2022;273:108741.

37. Said J, Fouvry S, Cailletaud G, Yang C, Hafid F. Shear driven crack arrest investigation under compressive state: Prediction of fretting fatigue failure of aluminium strands. Int J Fatigue. 2020;136:105589.